Supplementary Information (SI) for Materials Horizons.
This journal is © The Royal Society of Chemistry 2024

Supporting Information

Guided Ad infinitum Assembly of Mixed-Metal Oxide Arrays from Liquid Metal

Julia J. Chang,[a] Chuanshen Du,[b] Dhanush Jamadgni,[a] Alana Pauls,[a] Andrew Martin,[a] Le Wei,[c] Thomas Ward,[d] Meng Lu,[c] and Martin M. Thuo[a]*

[a] *North Carolina State University, Department of Materials Science & Engineering. Raleigh, NC 27695. United States.*
[b] *Iowa State University, Department of Materials Science & Engineering. Ames, Iowa 50011. United States.*
[c] *Iowa State University, Department of Electrical and Computer Engineering. Ames, Iowa 50011. United States.*
[d] *Iowa State University, Department of Aerospace Engineering. Ames, Iowa 50011. United States.*

E-mail: mthuo@ncsu.edu

Background

Lithography, the most widely used fabrication platform in electronic manufacturing, relies on selective deposition or abstraction of materials to create organized structures for a myriad of applications.[1] Lithographic methods fall into two main categories, *viz;* i) top-down, and ii) bottom-up methods. Top-down methods deploy physical- (e.g. e-beam lithography, photolithography, soft-lithography) or chemical- (wet or dry) abstraction to create patterns on generally hard materials (e.g. semiconductor, glass, metal). Top-down methods are widely used in fabrications of electronics,[2, 3] microfluidic chips,[4, 5] optical devices,[6-8] among others.[9, 10] In contrast, bottom-up approach is based on cross-linking (primary bonds) or organization/self-assembly (secondary/tertiary bonds) of individual building blocks across length scales.[11, 12] Depending on size and property of the building block, bottom-up methods generally give higher resolution.[13-15] Top-down and bottom-up strategies are also combined to enhance efficiency and accuracy of traditional lithography. [16, 17] Although complex instrumentation, strict operating conditions and sophisticated design are often required, top-down lithography is a powerful tool to create monolithic device functionalized by periodic patterns (e.g. gratings, waveguides, masks). However, to fabricate devices of which strict restrictions are set for the synergy of active unit, supportive part as well as substrate (MOSFETs, BJT, even a P-N junction diode), multiple steps of precisely controlled lithography are inevitable, which is energy intensive, capital intensive, and often require skilled manpower. At the same time, commercial electronic devices fabricated by bottom-up lithography as well as their mass production seem still out of reach. For the lithographic processes employing autonomous processes like capillary action and evaporation [18-20] or dynamic reactions,[21] more often serves as an assisting step to guide the lithography of the as-synthesized unit blocks. The prerequisite for unit block preparation as well as limitations in positional precision, compositional complexity, and morphological multiplicity hinder these methods merging into the current electronic fabrication industry. We therefore foresee that a high-precision autonomous bottom-up process as described here opens new pathways to fabricate advanced assemblies without analogous limitations in cost (millions of dollars for a fab-facility), training, characterization, etc that has translated Moore's law into 'More law' (Plot S1).

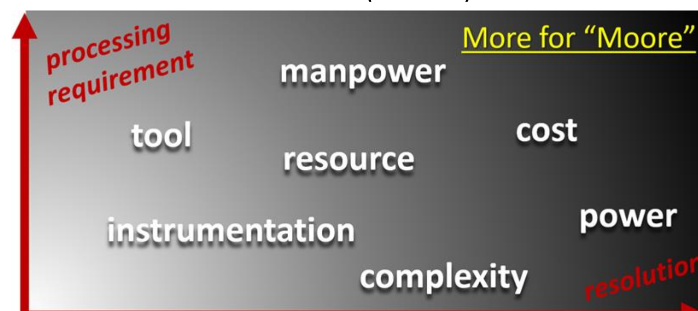

Plot S1: Increase in resource demand in fabrication of micro-electronics leading to Moore laws translating to"more" law.

Supporting Theory:

Consider a rectangular channel of length L (x direction) and height H (y direction) where $H/L \ll 1$. The liquid (solvent) and metal adduct (particle) mixture that initially fills the channel may be considered a thin film in this limit. The mixture fills the channel with solvent mass-fraction (mass/mass) denoted ϕ_s and metal adduct particle mass fraction denoted $\phi_m = 1 - \phi_s$. Since the adduct agglomerates are denser than the liquid, they settle in the channel forming a stratified layer of the solvent on top of mostly adduct—beside liquid that may be trapped in the particle's interlayer regions. The vapor-liquid interface profile for a liquid that fills a rectangular channel has a shape akin to that of the channel, thus the z profile (3rd direction), is nearly uniform except at the 3-phase contact line. We, therefore hypothesize that the liquid in the channel can be treated as a 2 dimensional thin-film, and assume that the constituent local-mass fractions vary with time and space as $\phi_s = \phi_s(x,t)$ and $\phi_m = \phi_m(x,t)$. The solvent-layer profile maintains a shape similar to a composite Heaviside function $H(x) - H(x-L)$ for $0 \leq x \leq L$ during evaporation, but with a magnitude that decreases with time as mass is transported from the liquid to vapor.[22]Here we assume the rate of change for the interface varies with time according to $\beta(t) = \beta_0 - \beta_1(t)$, where constant β_0 is the liquid initial height at time $t = 0$. We now write the interface profile as $h(x,t) = \beta(t)[H(x) - H(x-L)]$ for $0 \leq x \leq L$ and $t \geq 0$. Under limited Marangoni flow the interface shear stress is zero i.e. $\partial u/\partial y = -\partial v/\partial x$ [2] where these derivatives are evaluated at the vapor-liquid interface $y = h(t)$;[23] and the interface profile evolves according to $v = \partial h/\partial t + J/\rho$ [2]. Here $J = D\boldsymbol{n} \cdot \boldsymbol{\nabla} c$ is the flux of solvent into the vapor phase where $\boldsymbol{n} \cdot \boldsymbol{\nabla} c$ is computed at the gas-liquid interface $y = h(t)$ with outward point normal $\boldsymbol{n} = \boldsymbol{\nabla}(y - h(x,t))/|\boldsymbol{\nabla}(y - h(x,t))|$ and D denotes the solvent-vapor diffusivity,[24, 25] where c is the concentration (mass/volume) of solvent in the vapor-phase. Furthermore, the concentration gradient computed at the interface $y = h(t)$ is a function of x and t only; and we therefore let $\boldsymbol{n} \cdot \boldsymbol{\nabla} c = f(x,t)$ denote this gradient. Noting that the derivative of a Heaviside function is a delta function, it follows that $\partial[H(x) - H(x-L)]/\partial x = \delta(x) - \delta(x-L)$, where δ is the Dirac delta function, then we can express the streamwise velocity using an integral derived from shear stress $u = -\int_0^{h(t)} \partial v/\partial x$ after inserting expressions for $h(t)$ and J into the interface evolution equation. This yields a streamwise velocity $u = [-\beta_1[\delta(x) - \delta(x-L)] - D(df/dx)/\rho]y$. In the $H/L \ll 1$ limit the end channel regions that corresponds to $x = 0$ and $x = L$ are negligible. If we only consider the domain, $0 < x < L$, the equation reduces to;

$$u = -D[df/dx]y/\rho$$

Thus, the velocity u primarily drives flow to minimize gradients in $f(x,t) = \boldsymbol{n} \cdot \boldsymbol{\nabla} c$ i.e. larger df/dx results in larger u. We would normally need only to find solutions for the concentration profile by solving a Laplacian equation $\nabla^2 c = 0$ to estimate the velocity magnitude, but this is not necessary if we consider the combination of Raoult's law for the solvent-vapor concentration above the liquid as a function of liquid phase solvent concentration, and Dalton's law for the solvent-vapor pressure as a function of the total pressure. Combining these law's results in an expression for solvent concentration $c = \rho P_{vap} x_s/P$ where x_s is the solvent liquid phase mol

fraction that is related to the liquid phase mass fraction via $x_s = \phi_s/[[1-\phi_s](MW_s/MW_m) + \phi_s]$ where ϕ_s is the liquid phase solvent mass fraction, and ρP_{vap} is the solvent equilibrium vapor pressure. MW_s and MW_m denote the solvent and metal adduct molecular weights respectively. This relation directly implies precipitation with increase in molecular weight of the adducts. These expressions were derived assuming only two component liquid-solvent and metal adduct; the assumption is still valid for other mixtures as long as the solute/particle possess lower vapor pressure relative to the solvent. Using the chain rule we can write $df/dx = (dx_s/dx)\, df/dx_s$. The second derivative may be computed using the expression written here for x_s. One more application of the chain rule yields $dx_s/dx = (d\phi_s/dx)\, dx_s/d\phi_s$. Therefore, the velocity u appears to minimize gradients in solvent, and likewise in metal-adduct concentration. Use of nm to m wide channels and low viscosity fluids implies rapid channel filling as dictated by Jurin's law ($h = \frac{2\gamma cos\theta}{\rho g r_0}$). Initial profile, $h(x, t=0)$, may therefore affect precipitation based on Taylor dispersion where a particle layer may form due to initial filling of the channel by capillary forces.[26-28] But these would only enhance this flow through the transient profile gradient and normal i.e. an increase in magnitude for $|\partial[\partial h/\partial t]/\partial x|$. The scalar concentration gradient computed at the interface is $\boldsymbol{n} \cdot \boldsymbol{\nabla} c < 0$ for all time with zero initial solvent concentration in the vapor. Directed evaporation, however, becomes a paramount condition for controlled uniform growth of these polymerizing adducts.

Materials and Methods:

Materials: Field's metal (FM, eutectic indium 51 wt%–bismuth 32.5 wt%–tin 16.5wt%) and tin metal were purchased from Rotometals. Indium metal (99.999%) was from Alfa Aesar. Glacial acetic acid (99.7%), trichloroacetic acid(99.8%), ethyl acetate (reagent grade, 99.9%), and acetone (HPLC grade, 99.7%) were from Fisher Scientific. Diethylene glycol (99.9%) was purchased from VWR. Ethanol (anhydrous) was from Decon laboratories Inc. Above supplies were used as received. Deionized water was prepared using a Thermo Scientific Smart2Pure® 6 UV water purifier system. Si substrates (University wafers) and glass slides (J. Melvin Freed brand) were used after cleaning with ethanol. Polydimethylsiloxane (PDMS) gratings were prepared by soft lithographic replication from a glass grating and cut with scissor or blade orthogonal to the length of the channel to expose inlets or outlets.

Imaging: For imaging purpose, wires made with open channel process were lifted off with Cu tape then adhered to a flat scanning electron microscopy (SEM) stub (Ted Pella, Inc.). Wires on Si substrate were imaged directly after adhering to an SEM stub. Morphology characterizations were done using an FEI-SEM Quanta 250 with 3.0 a.u. spot size and 10 mm working distance. For calcined wires, the working voltage was 10.0 kV while pristine wires were imaged at lower voltage (7.0 kV). Back Scattered electron (BSE) detector was used to differentiate beam and substrate. Composition analysis was carried out using energy dispersive X-ray spectroscopy (EDS). For element mapping, spot size of 5.0 a.u. was used to improve signal quality, while a 4.0 spot size was chosen where higher resolution was desired.

X-Ray Powder Diffraction (XRD): XRD was done on calcined wires detached from Si substrate. Ground beam powder was spread onto zero diffraction substrate with a thin Vaseline® layer. Sample were characterized by Siemens® D500 x-ray with a copper X-ray tube. Phase identification and pattern fitting were done using the Jade® software.

Focused Ion Beam (FIB): FIB milling of the formed structures was done on the Thermo-Fisher Helios Hydra G5 DualBeam Plasma FIB. The sample (on Si wafer) was mounted on a standard SEM stub using carbon tape. FIB milling was done on eucentric height of 4 mm using an Ar primary ion beam at 30 kV accelerating voltage and 60 pA current. Imaging was performed using a Ion Conversion and Electron (ICE) secondary electron detector at 10 kV and 1.6 nA.

X-ray Photoelectron Spectroscopy (XPS): XPS characterization was performed on a Thermoscientific NEXSA G2 instrument using the Avantage software. The thin film samples were mounted on a flat mount and the powder samples were mounted on the well mount. At least 3 spots were analyzed for each sample. XPS survey spectra was collected once for each sample with binding energy ranging from -10.00 eV to 1350.000 eV, pass energy – 200 eV, number of scans – 2, dwell time – 10ms, energy step size of 1eV. Further at each point Bi(4f), C(1s), In(3d), Sn(3d), O(1s) elements were collected with binding energy 148.0-172.0eV, 274.0-302.0eV, 433.0-465.0eV, 474.0-505 eV, 520.0-550.0eV respectively. All scans were done with pass energy of 50eV, 15 scans, dwell time of 50ms and with an energy step size of 0.1eV. The atomic concentration of elements was determined from the integrated intensity of the elemental photoemission features corrected by relative atomic sensitivity factors and the chemical states of elements were assigned based on the PHI and NIST XPS Databases.

Atomic Force Microscopy (AFM): AFM images were collected using a Digital Instruments (now Bruker®) Multi-Mode AFM in contact mode with sharp nitride lever (SNL) probes. The feature height, width and cross section spectrum were analyzed automatically using the integrated Nanoscope Analysis v2.0 Software.

Construction of simplified Back gate field-effect transistor (FET): Back-gate FET was constructed by connecting gold electrodes to ends of wire arrays as source and drain electrodes. Si substrate was used as back-gate electrode and the intrinsic SiO_2 layer on Si substrate served as dielectric in the FET device. 1 to 5 V voltage was applied on Si substrate. Under each applied voltage, current between source and drain was recorded versus the source-gate voltage changed from -4 to +4 V in a step of 0.1V. The measurement was done using HP 4155B semiconductor analyzer with a probe station.

Transmission spectrum measurement: The transmission spectra of pristine arrays on glass were measured using a homebuilt device. After mounting the sample on stage, a collimated broadband light (HL-2000, OceanOptics) was applied as light source and shined vertically on sample. Transmitted light was collected by fiber and analyzed by OceanOptics USB2000 spectrometer.

Electromagnetic simulation: The Rigorous coupled-wave analysis (RCWA) simulations were performed using a commercial modeling tool (DiffractMOD, Synopsys). The simulation domain included only one period of the 1D structures with the periodic boundary conditions to truncate

the 1D grating at the x -axis.The refractive index (n(λ)) and extinction coefficient (k(λ)) of film were interpolated using the results obtained from the ellipsometry measurement. The incidence of plane-wave was linearly polarized along the x-axis and y-axis. The transmission spectra were calculated in the wavelength range of 400 nm to 800 nm. At the resonance wavelength, the electric field (|E/Einc|2) distributions in the simulation domain were calculated.

Supporting Discussion

1. Calculation of fluxing agent physical properties

For a binary liquid mixture, if only laminar interaction of flux and capillary channel was considered, surface tension of solution was estimated by assuming additivity: $\gamma = X_1\gamma_1 + X_2\gamma_2$.[29] If fluxing agent was treated ideally, viscosity could be calculated using the Arrhenius equation: $ln\, ln\, \eta\ = ln\, X_1 ln\, \eta_1\ + ln\, X_2 ln\, \eta_2$.[30] Mixture vapor pressures were calculated from Raoult's law: $P =\ X_1P_1 + X_2P_2$. X_i, γ_i, η_i and P_i are the mole fraction, surface tension, viscosity, and vapor pressure for pure components (Dortmund Data Bank, wwww.ddbst.com). Obtained results are summarized in Table S1.

Table S1. Physical properties of fluxing agent at 293.15 K

Activation agent	Surface tension γ (mN/m)	Contact angle θ on PDMS (˚)	Viscosity η (mPa·s)	Penetrativity p (m/s)
AcOH/Ace	25.55	40.32±1.78	0.68	14.27
AcOH/EtOH	24.83	45.76±1.04	1.20	7.23
AcOH/H2O	61.89	76.08±1.50	1.05	7.08

2. Calculation of Resistance

Resistance reciprocal was calculated using 1st derivative of linear part in last-cycle I-V curve. Then resistivity and conductivity of wires was calculated by using obtained resistance and wire dimension parameters from AFM and SEM data.

3. Back-gate FET threshold voltage calculation

The threshold voltage V_T of FET devices were calculated by equation:

$$V_T = V - V_{D-S_SAT}$$

V is the voltage applied on the substrate while V_{D-S_SAT} is the saturation source-drain voltage. For estimation, the value of V_{D-S_SAT} was found by taking the 1-st derivative of I_{S-D} versus V_{S-D} curves then using the voltage at valley point as V_{D-S_SAT}. The valid V_{D-S_SAT} values for V=2, 4,5 V were 0.8, 1.5 2.3 V for calcined FM wires and 1, 1.8 2.4 V for calcine IT wires.

Supporting Figures

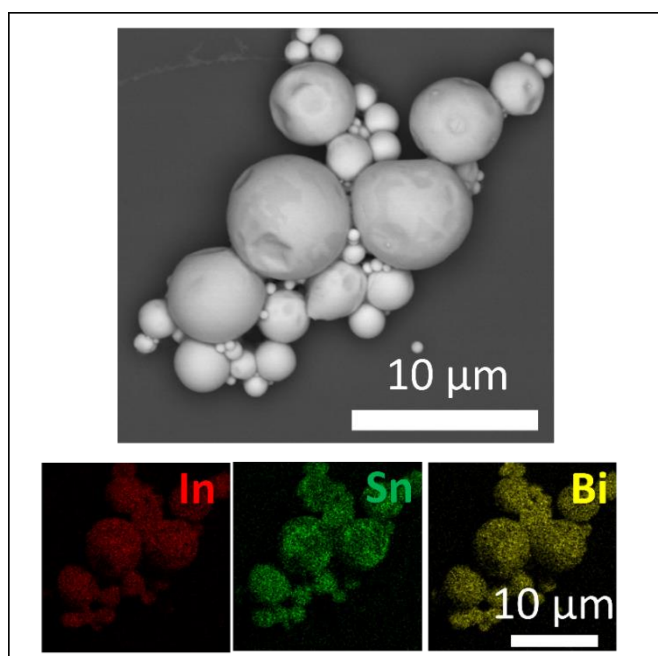

Figure S1. SEM and EDS results of undercooled Field's metal particles.

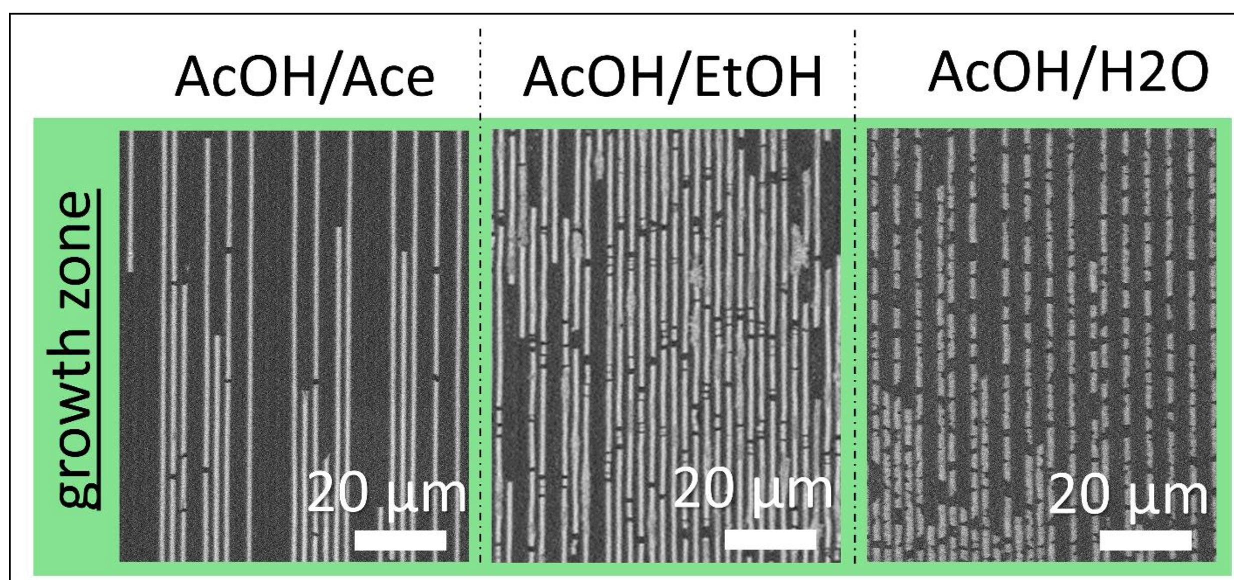

Figure S2. SEM images of polydimethysiloxane (PDMS) gratings applied in this study.

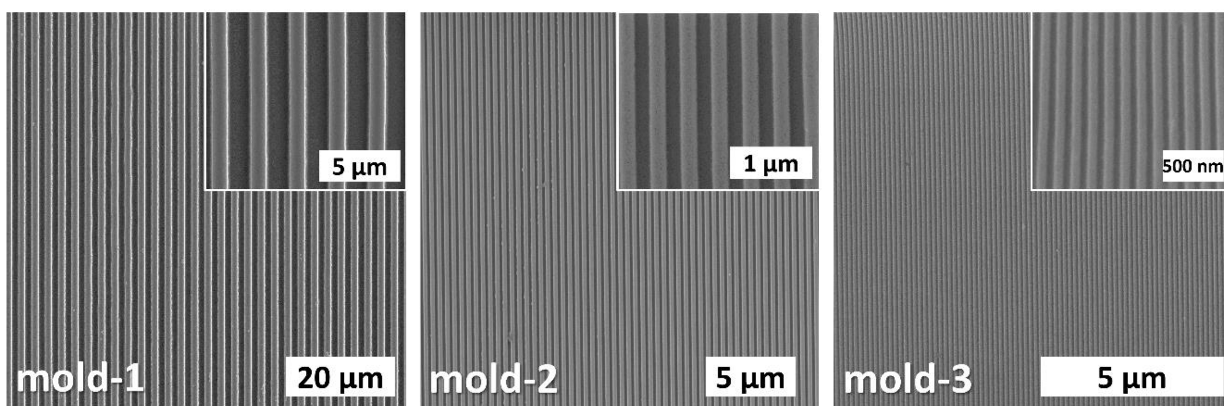

Figure S3. SEM images of Field's metal nanowire arrays generated in grwoth zone by applying different activation solvents.

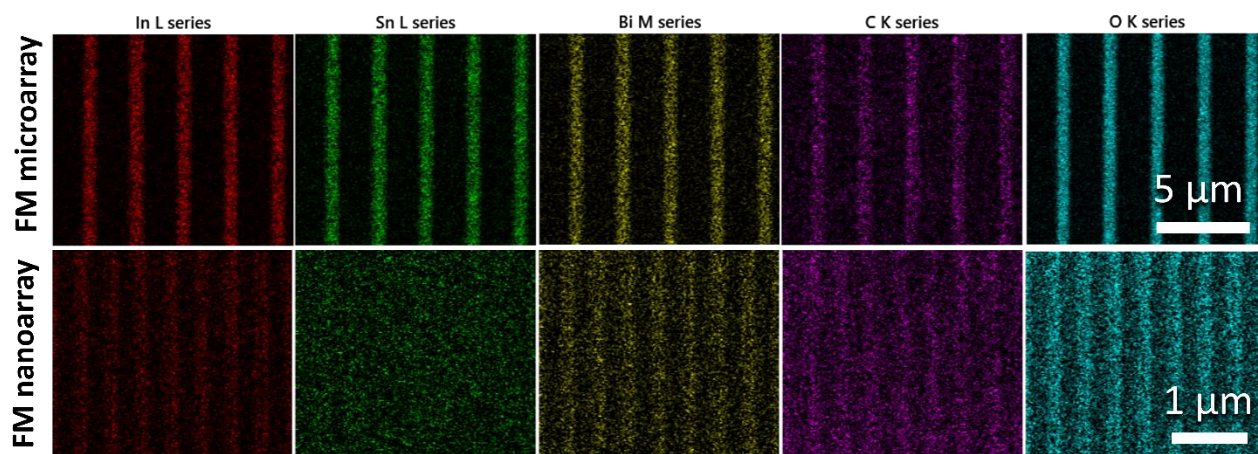

Figure S4. EDS mapping of Field's metal D-Met micro- and nano-arrays.

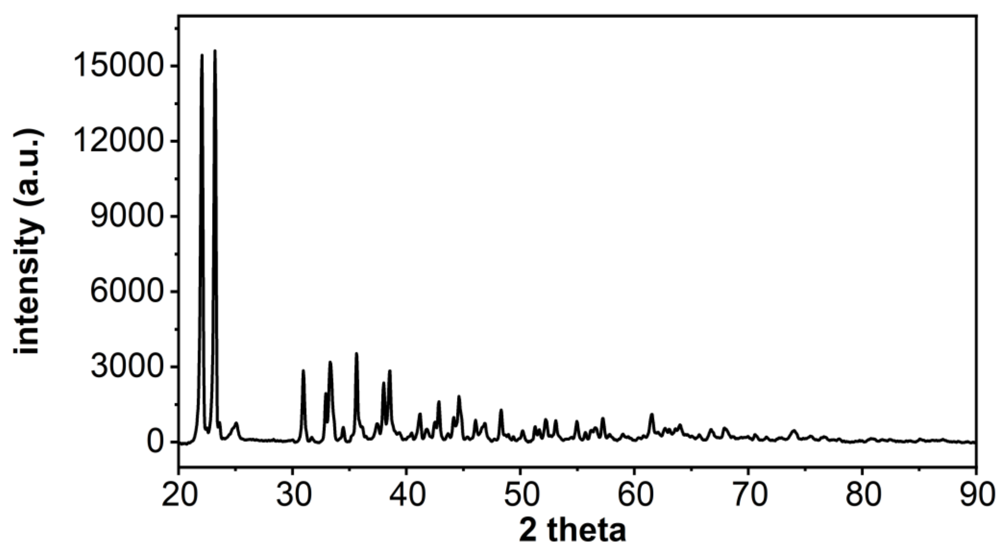

Figure S5. XRD spectrum of Field’e metal pristine HetMt reaction product.

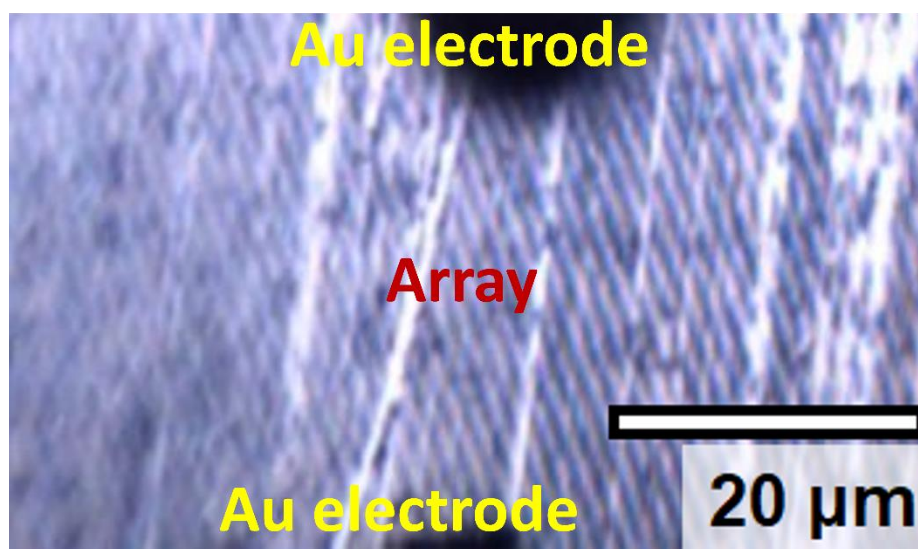

Figure S6. Photo of electrical measurement system showing the placement of the electrodes on the array.

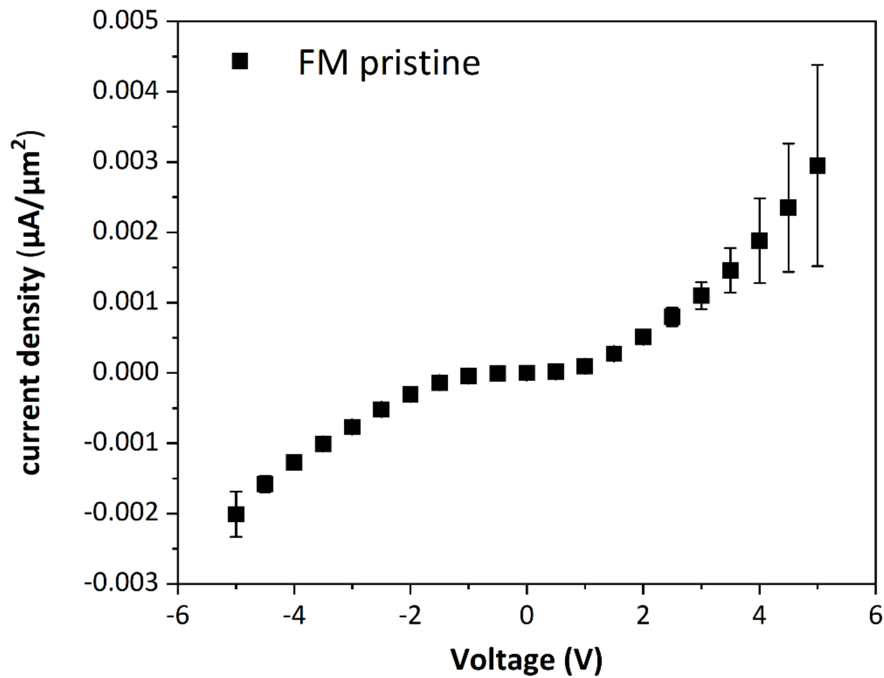

Figure S7. I-V curve of pristine Field's metal D-Met array with coordinates adjustment.

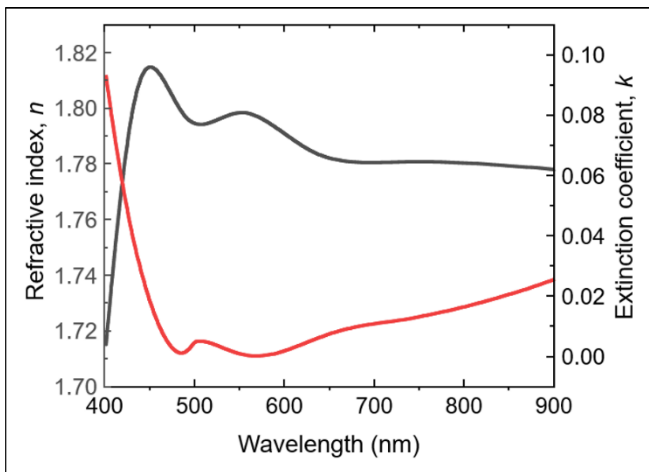

Figure S8. Refractive index n and extinction coefficient k spectra of pristine nanowire arrays made with indium tin particles.

Reference

1. Thompson, L.F., *An introduction to lithography*. 1983, ACS Publications.
2. Chen, M.-L., et al., *A FinFET with one atomic layer channel.* Nature Communications, 2020. **11**(1): p. 1-7.
3. Im, H., et al., *A dielectric-modulated field-effect transistor for biosensing.* Nature Nanotechnology, 2007. **2**(7): p. 430-434.

4. Dendukuri, D., et al., *Continuous-flow lithography for high-throughput microparticle synthesis.* Nature Materials, 2006. **5**(5): p. 365-369.
5. Nie, Z., et al., *Electrochemical sensing in paper-based microfluidic devices.* Lab on a Chip, 2010. **10**(4): p. 477-483.
6. Henzie, J., M.H. Lee, and T.W. Odom, *Multiscale patterning of plasmonic metamaterials.* Nature Nanotechnology, 2007. **2**(9): p. 549-554.
7. Li, J., et al., *A reusable metasurface template.* Nano Letters, 2020. **20**(9): p. 6845-6851.
8. Yang, W., et al., *All-dielectric metasurface for high-performance structural color.* Nature Communications, 2020. **11**(1): p. 1-8.
9. Qin, D., Y. Xia, and G.M. Whitesides, *Soft lithography for micro-and nanoscale patterning.* Nature Protocols, 2010. **5**(3): p. 491.
10. Whitesides, G.M., et al., *Soft lithography in biology and biochemistry.* Annual Review of Biomedical Engineering, 2001. **3**(1): p. 335-373.
11. Bowden, N., et al., *Self-assembly of mesoscale objects into ordered two-dimensional arrays.* Science, 1997. **276**(5310): p. 233-235.
12. Zhang, J., et al., *Colloidal self‐assembly meets nanofabrication: From two‐dimensional colloidal crystals to nanostructure arrays.* Advanced Materials, 2010. **22**(38): p. 4249-4269.
13. Cademartiri, L. and K.J. Bishop, *Programmable self-assembly.* Nature Materials, 2015. **14**(1): p. 2-9.
14. Nie, Z., A. Petukhova, and E. Kumacheva, *Properties and emerging applications of self-assembled structures made from inorganic nanoparticles.* Nature Nanotechnology, 2010. **5**(1): p. 15-25.
15. Yang, F., et al., *Laser‐Scanning‐Guided Assembly of Quasi‐3D Patterned Arrays of Plasmonic Dimers for Information Encryption.* Advanced Materials, 2021. **33**(24): p. 2100325.
16. Huo, F., et al., *Beam pen lithography.* Nature Nanotechnology, 2010. **5**(9): p. 637-640.
17. Wang, Y., et al., *Direct optical lithography of functional inorganic nanomaterials.* Science, 2017. **357**(6349): p. 385-388.
18. Ni, S., L. Isa, and H. Wolf, *Capillary assembly as a tool for the heterogeneous integration of micro-and nanoscale objects.* Soft Matter, 2018. **14**(16): p. 2978-2995.
19. Probst, P.T., et al., *Mechano-tunable chiral metasurfaces via colloidal assembly.* Nature Materials, 2021. **20**(7): p. 1024-1028.
20. Xu, J., et al., *Multi-scale ordering in highly stretchable polymer semiconducting films.* Nature Materials, 2019. **18**(6): p. 594-601.
21. Lagzi, I., B. Kowalczyk, and B.A. Grzybowski, *Liesegang rings engineered from charged nanoparticles.* Journal of the American Chemical Society, 2010. **132**(1): p. 58-60.
22. Erturk, A. and D.J. Inman, *A distributed parameter electromechanical model for cantilevered piezoelectric energy harvesters.* Journal of vibration and acoustics, 2008. **130**(4).
23. Hu, H. and R.G. Larson, *Marangoni effect reverses coffee-ring depositions.* The Journal of Physical Chemistry B, 2006. **110**(14): p. 7090-7094.
24. Hu, H. and R.G. Larson, *Analysis of the effects of Marangoni stresses on the microflow in an evaporating sessile droplet.* Langmuir 2005. **21**(9): p. 3972-3980.

25. Hu, H. and R.G. Larson, *Analysis of the microfluid flow in an evaporating sessile droplet.* Langmuir, 2005. **21**(9): p. 3963-3971.
26. Taylor, G.I., *Dispersion of soluble matter in solvent flowing slowly through a tube.* Proceedings of the Royal Society of London. Series A. Mathematical and Physical Sciences, 1953. **219**(1137): p. 186-203.
27. Aris, R., *On the dispersion of a solute in a fluid flowing through a tube.* Proceedings of the Royal Society of London. Series A. Mathematical and Physical Sciences, 1956. **235**(1200): p. 67-77.
28. Balog, S., et al., *Taylor dispersion of nanoparticles.* Journal of Nanoparticle Research, 2017. **19**(8): p. 1-11.
29. Shereshefsky, J., *A theory of surface tension of binary solutions: I. Binary liquid mixtures of organic compounds.* Journal of Colloid Interface Science, 1967. **24**(3): p. 317-322.
30. Anantaraman, A., *Thermodynamics of solvent mixtures. I. Density and viscosity of binary mixtures of N-methylpyrrolidinone–tetrahydrofuran and propylene carbonate–acetonitrile.* Canadian journal of chemistry, 1986. **64**(1): p. 46-50.